Engineering Structures 304 (2024) 117610

Contents lists available at ScienceDirect

Engineering Structures

journal homepage: www.elsevier.com/locate/engstruct

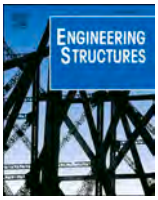

Experimental and analytical study on the behaviour of circular concrete filled steel tubes in cyclic bending

Rosario Montuori [b], Elide Nastri [a,*], Vincenzo Piluso [a], Paolo Todisco [a]

[a] Department of Civil Engineering, University of Salerno, Fisciano, SA, Italy
[b] Department of Pharmacy, University of Salerno, Fisciano, SA, Italy

ARTICLE INFO

Keywords:
CFTs
Steel
Concrete
Numerical model
Experimental

ABSTRACT

In the present study, a comprehensive experimental investigation is conducted on eight Concrete-Filled Tube (CFT) specimens subjected to bending loads under cyclic conditions. The loading regimes included constant and variable amplitude cycles. Strain was precisely measured using strategically placed gauges, and the data generated load-displacement and moment-curvature curves. A novel analytical model is developed and calibrated to match the experimental outcomes; this model incorporates the Mander stress-strain relationship for confined concrete and the Ramberg-Osgood model for steel. The study provides new insights into the mechanical behaviour of CFTs under bending, particularly in terms of strain distribution, load-displacement characteristics, and failure modes. This research serves as a strong foundation for future finite element modelling and design optimization of CFT structures, enhancing their safe and efficient use in engineering applications.

1. Introduction

In the realm of structural engineering, Concrete-Filled Tubes (CFTs) have emerged as a crucial innovation, attracting considerable research and practical attention due to their composite material constitution. This system is achieved by the in-situ casting of concrete into a longitudinally-welded steel tube, thereby forming an integrated composite element that capitalizes on the mechanical properties of both steel and concrete. The application spectrum of CFTs is extensive, spanning various sectors of civil engineering infrastructure such as high-rise commercial and residential buildings, bridge substructures, and offshore platforms. One of the inherent advantages of CFTs is their enhanced fire resistance, which is primarily a function of the thermal insulating properties of the concrete core. This characteristic significantly improves the column's fire load-bearing capacity, thereby reducing the risk of structural failure under fire exposure conditions.

From a mechanical standpoint, the interaction between the steel tube and the concrete core in CFTs is of paramount importance. The steel tube not only acts as a formwork during the concrete casting but also provides lateral confinement to the concrete core under axial loads. This confinement effect significantly enhances the axial load-carrying capacity of the composite column and delays the onset of material yielding and local buckling. Moreover, the steel tube effectively acts as an external reinforcement, thereby improving the column's flexural stiffness and ductility. Additionally, the composite action between the steel and concrete components mitigates the susceptibility of the column to global buckling, particularly in slender configurations. This is achieved through the increased moment of inertia provided by the composite section, which in turn improves the column's buckling resistance. CFTs offer a multifaceted structural solution that amalgamates the beneficial properties of steel and concrete. Their composite nature not only enhances mechanical performance but also provides inherent fire resistance and buckling mitigation, making them a highly effective and versatile element in modern structural engineering applications [1,2].

In high-rise buildings, CFTs contribute to structural resilience by offering enhanced load-carrying capacity, stiffness, and ductility. Their composite nature allows them to efficiently resist both gravity and lateral forces, making them particularly suitable for tall structures that are subjected to wind and seismic actions. In the realm of bridge construction, CFTs offer robustness and durability, capable of withstanding dynamic loads and harsh environmental conditions. They are particularly effective in dissipating and distributing dynamic forces, thereby enhancing the overall seismic performance of bridges. Notable examples of CFT applications include the Canton Tower in Guangzhou, which stands as a testament to the innovative use of CFTs in high-rise construction. The tower structural system incorporates CFTs to provide the

* Corresponding author.
E-mail address: enastri@unisa.it (E. Nastri).

https://doi.org/10.1016/j.engstruct.2024.117610
Received 9 November 2023; Received in revised form 21 December 2023; Accepted 30 January 2024
Available online 14 February 2024

necessary strength, stability, and load-carrying capacity. Another example is the Wang Chang East River Bridge in Sichuan Province, China, which demonstrates the effectiveness of CFTs in bridge construction with a span of 115 m. Internationally, the iconic Petronas Towers in Kuala Lumpur, Malaysia, employ CFTs in their structural design to support their immense height and loads. Similarly, the Taizhou Bridge in China, one of the longest cable-stayed bridges in the world, utilizes CFTs in its bridge towers and piers for strength and stability.

Design guidelines and codes, such as those provided by the American Concrete Institute (ACI) [3], the American Institute of Steel Construction (AISC) [4], and Eurocode provisions [5], offer comprehensive recommendations for the design and analysis of concrete-filled tubes. These guidelines consider factors such as material properties, member dimensions, and safety requirements, ensuring reliable and efficient design practices, but are mainly focused on the axial behaviour.

Various studies have explored CFTs structural behaviour, assessing the impact of factors like steel thickness, concrete strength, and steel-concrete bond on CFT performance [6]. Research have been conducted mainly on the axial behaviour of concrete-filled tubes (CFTs) [7,8], ranging from experimental testing to the development of predictive analytical models. Experimental investigations have specifically focused on both simple CFTs [9,10] and fibre-reinforced CFTs [11–13]. These reinforcement attempts, arise from the analysis of the interaction between steel and concrete [13]. The different material characteristics in the elastic phase are examined by various researchers, suggesting that this phenomenon leads to an incomplete utilization of the mechanical properties of the composite element, as stated by Lai et al. [14].

In addition to extensively researching the axial behaviour, some research has also delved into the torsional behaviour of CFTs, indicating a need for further detailed study [15,16]. Regarding the flexural behaviour, Elchalakani et al. [17] pioneered research on monotonic flexural behaviour in circular CFTs, analysing a wide d/t ratio range (from 12 to 110). A subsequent study by the same group [18] extended the analysis to cyclic bending behaviour, focusing on failure modes and moment-cycle evolution, but omitted moment-curvature details. The limitation of these studies lies in analysing CFTs with dimensions significantly different from practical operational use, considering only constant amplitude tests. Deng et al. [19] further contributed by examining the impact of post-tensioning on the flexural behaviour of steel circular CFTs. Moreover, Zhou et al. [20] contribute an experimental analysis focusing on the mechanical attributes of CFSTs when filled with ultra-high-strength concrete, thereby pushing the boundaries of material capabilities. Deng et al. [21] and Li et al. [22] extend this line of inquiry by evaluating the flexural performance of CFSTs constructed with both ultra-high-performance concrete and high-strength steel tubes, likely incorporating both experimental and computational methodologies to elucidate structural behaviour and failure mechanisms. Ou et al. [23] offer a novel approach by investigating the flexural enhancements achieved through the external strengthening of circular CFSTs with Carbon Fiber Reinforced Polymer (CFRP) sheets, potentially offering a pathway for retrofitting existing structures.

The works of İlgün et al. [24] and Abed et al. [25] provide a comparative analysis of the flexural behaviour of CFSTs with varying cross-sectional geometries and concrete types, thereby offering insights into design optimization.

Lastly, advanced research has been conducted by Ding et al. spanning from the behavior of CFTs subjected to high axial force values to more detailed scenarios, such as their application in bridge elements [26–29].

As is clear from the previously mentioned works, the studies following Elchalakani et al.[18] have delved into more detailed aspects without, however, addressing the highlighted deficiencies.

This study addresses a gap in the current literature by focusing on the cyclic flexural behaviour of CFTs under both constant amplitude (CA) and variable amplitude (VA) loading. While existing studies have primarily examined monotonic loading and material properties, this research provides a comprehensive analysis of CFTs under cyclic loading conditions. A particular gap that has been filled is the testing of CFTs with dimensions closer to practical use, unlike previous studies where they were scaled down without considering potential scale effects.

Moreover, a fibre model to predict the bending-curvature behaviour of CFTs is proposed as alternative to those developed by Liang et al. [30] and Fujimoto et al. [31].

Eight specimens, designated C1-C8, were subjected to a series of experimental tests involving both monotonic and cyclic loading in bending. The tests yielded data on load-deformation responses, failure modes, and ultimate strength, contributing to the understanding of CFT structural response under varied loading conditions.

To supplement the experimental data, a numerical model was developed to simulate moment-curvature behaviour. This model incorporates the material properties and non-linear behaviour of both steel and concrete, adding a layer of complexity often missing in existing models. The study also includes a detailed cycle-by-cycle analysis of curvature, energy dissipation, and degradation, covering a range of width-to-thickness ratios (d/t) from approximately 25 to 50. The experimental and numerical results were compared to validate the model reliability and accuracy.

The innovative aspect of this study lies in its focus on cyclic loading conditions and its integration of both experimental and numerical methods. This dual approach provides a more comprehensive understanding of CFT behaviour, offering valuable insights for future research and practical applications in composite structure design.

The paper is structured into five main sections. Section 2 provides a detailed description and execution of the specimens used in the study. Section 3 elaborates on the experimental tests conducted on CFTs, while Section 4 focuses on the bending moment-curvature relationship, bridging experimental results to a fibre numerical model. Finally, Section 5 offers the study conclusions.

2. Description and execution of specimens

This section offers an exhaustive delineation of the CFTs, encompassing both the methodologies employed in their fabrication and the mechanical characterization of the constituent materials. The experimental setup and associated test protocols are systematically outlined. Additionally, the mechanical attributes of the individual components, namely the concrete core and the encasing steel tubes, are rigorously assessed through a series of specialized tests. In accordance with the pre-

Fig. 1. Execution of the specimens.

established experimental schema, two distinct groups of CFT columns were subjected to testing, as depicted in Fig. 1. The first group, designated as Group 1, consisted of specimens labelled C1 through C4, while the second group, designated as Group 2, included specimens labelled C5 through C8. These CFT columns were constructed using steel elements with mechanical properties analogous to those of S355-grade steel. The primary variable under investigation among the tested specimens was the width-to-thickness ratio (D/t).

The steel tubes used in the experiments were fabricated from longitudinally welded, cold-formed steel plates. Group 1 tubes had an outer diameter ranging from 313.0 to 319.0 mm, a height of 2400 mm, and a wall thickness varying between 6.5 and 9.5 mm. A 30 mm thick plate was welded to one end of each tube, occluding the base, while the other end featured an additional plate of the same diameter with a cavity matching the tube diameter.

Group 2 tubes had an outer diameter (D) ranging from 249.2 to 260.4 mm, a height (h) of 2400 mm, and a wall thickness (t) varying between 6.1 and 10.6 mm. Both ends of these tubes were welded with 20 mm thick plates. The geometry is summarized in Table 1. It is pointed out that each experimental condition was replicated across two specimens, C1 and C2, as well as C3 and C4, thereby allowing us to assess the repeatability and stability of the results and confirm that the observed behaviours were stable. Internal consolidation of the concrete was accomplished using a vibrating poker. Finally, the specimens were carefully stored for an appropriate duration to ensure proper curing.

3. Description and execution of the experimental tests on CFTs

The specimens from Groups 1 and 2 underwent both cyclic and monotonic three-point bending tests. In Group 1, the specimens were subjected to tests employing constant amplitude loading profiles. Conversely, the specimens in Group 2 were subjected to tests with both constant amplitude and variable amplitude loading, as well as varying loading rates. Notably, no axial load was applied to the specimens, as the experimental focus aimed to simulate the response of bridge piles, which typically experience axial loads representing only 10% of their ultimate axial load capacity.

The tubes were extracted from their storage location for seasoning and, with the assistance of an overhead gantry crane, were positioned on the base of the hydraulic actuator (Figs. 2 and 3).

Articulated pins were affixed at both beam ends (Fig. 4) using two plates secured by 10 M25 bolts each, tightened to 340 Nm torque via a dynamometric wrench with a 30 mm hex socket. These pins were anchored to the machine platform with eight M22 bolts each, allowing specimen ends to rotate in-plane and achieve a simply supported configuration.

The bolts at the base of the hinge were loosened on one side to provide a degree of freedom (horizontal displacement) to transform the hinge into a slider and avoid any potential influence on the test results. The resulting configuration is that of a beam with a pinned support at each end and a slider with a mid-span force. The load was applied at the centre of the specimen using a hydraulic actuator with a capacity of 2500 kN in tension and 3000 kN in compression. The connection between the specimen and the actuator was achieved using a shaped, semi-cylindrical hollow element (Fig. 5) with a diameter matching that of the steel tube. It was placed at the centre of the specimen and tightened with its symmetrical counterpart through three bolts per side, ensuring a conforming fit to the specimen, and creating a rigid stub (Fig. 5).

The displacement and deformation measurement instruments (Fig. 6) were set up differently for the two groups of CFT (Concrete-Filled Tube). For Group 1, four Linear Variable Differential Transformers (LVDTs) were utilized to measure displacements on each test story. Two LVDTs, capable of 10 cm stroke, were positioned above the specimen, spaced 18 cm from the bases, while the other two, with a 5 cm stroke, were positioned below the specimen, spaced 3 cm from the bases. Strain gauges were affixed using a specialized adhesive, precisely at a distance of 10 cm from the piston, facilitating strain measurement.

For Group 2, supplementary sensors were strategically placed along the specimens, following meticulous calibration, to ensure precise displacement measurement for each. Specifically, in each test, three 500 mm wire sensors were positioned at the mid-span of the specimen and at the midpoints of both halves of the CFT. For Group 1 (C1-C4) the specimens were subjected to cyclic testing at constant amplitude (0–220 mm). For Group 2, the specimens called C5 and C7 were subjected to cyclic testing at constant amplitude (0–140 mm), while the C6 and C8 specimens were subjected to cyclic testing at increasing amplitude (Table 2) [4]. Constant amplitude tests were set up to assess cyclic degradation and collect data regarding the damage function. Variable amplitude tests were conducted to evaluate hardening behaviour and the evolution of secant stiffness.

Table 1
Geometry of the CFT specimens.

Label	h [mm]	D [mm]	t [mm]	D/t [-]
Group 1				
C1	2400	319.0	9.5	33.58
C2	2400	319.0	9.5	33.58
C3	2400	313.0	6.4	48.91
C4	2400	313.0	6.4	48.91
Group 2				
C5	2400	249.2	6.1	40.85
C6	2400	260.4	10.4	25.04
C7	2400	249.4	6.2	40.23
C8	2400	255.2	10.6	24.08

4. Experimental results

4.1. Experimental tests on casted concrete

Pertaining to the concrete core, a C30/35 mix design was employed for the infill. The concrete was poured into a total of sixteen resin moulds, each with dimensions of 150×150×150 mm. Prior to casting, meticulous care was taken to clean the inner surfaces of the moulds, facilitating the application of a form release agent containing a surfactant, as illustrated in Fig. 7. After the casting process, each specimen was systematically labelled, subjected to a prescribed curing protocol and, after 28 days, evaluated through testing procedures.

The mean values of the failure force $F_{c.m}$ and the failure stress $f_{c.m}$ are reported in Table 3.

4.2. Description and results of the experimental tests on "Dog bones"

Post-testing, CFT columns were disassembled and two steel samples per column were extracted using an angle grinder. These samples were then milled into a "dog bone" shape.

The geometric characteristics of each specimen and the main parameters derived through the experimental uniaxial test in tension (Fig. 8), are provided in Table 4, where A_0 is the initial area of the specimen; A_f is the area at the end of the experimental test (available only for group 2); f_y is the yielding stress; $f_{\max}$ is the maximum stress; f_t is the stress at failure; $\varepsilon_{f_{\max}}$ is the strain corresponding to the maximum stress; ε_{f_t} is the strain corresponding to the failure of the specimen; E is the elastic modulus; L_0 is the gauge length. In brackets, the Abaqus notation is reported.

4.3. Results on CFTs specimens

The experimental results are synthesized through force-displacement curves that quantify the relationship between the total reaction force and the central deflection of the specimens (Fig. 9 for group 1 and Fig. 10 for group 2 specimens). These curves are directly extracted from

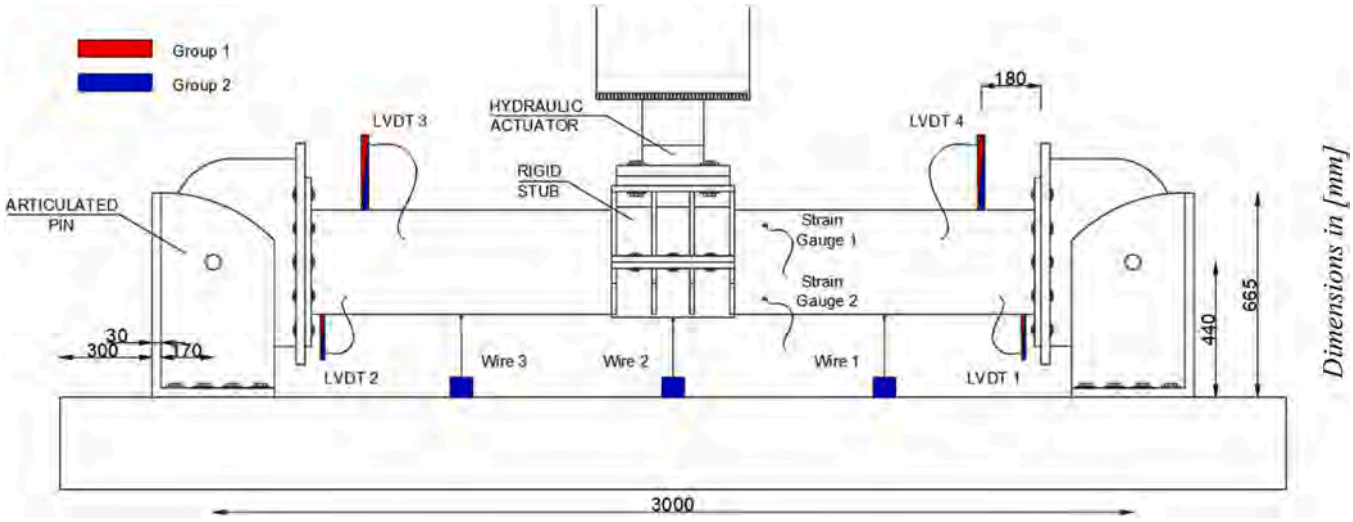

Fig. 2. Experimental setup scheme.

Fig. 3. Realization of the experimental setup.

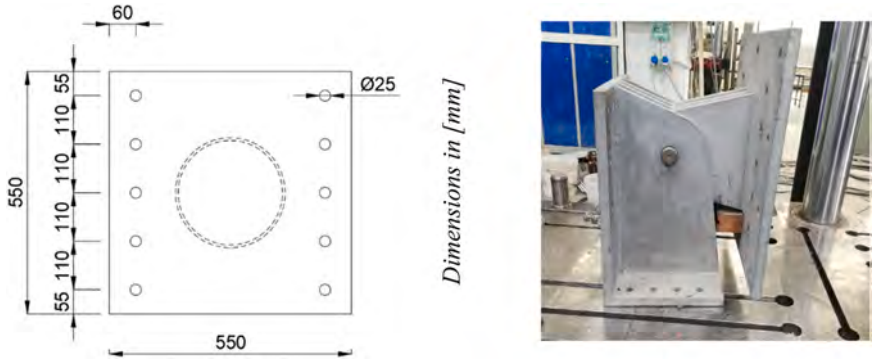

Fig. 4. Articulated end pin.

the actuator data output. Additional quantities such as the number of cycles, energy dissipated per cycle, cumulative damage function, and percentage of cumulative damage are also reported for all specimens.

Morphological anomalies, including two bulges and proximal cracks near the load cell attachment, have been observed for all the specimens (Fig. 11). The most prone failure mechanism involved steel fracturing and the ejection of pulverized concrete from within the CFT.

The C1 specimen presented a first loop not connected to the rest of the loops due to hydraulic actuator complications encountered during the experiment. Specifically, no data were recorded during the unloading phases around 125 mm. The actuator restarted from a displacement of 75 mm at midspan. The C2 specimen presented experimental complications due to restricted horizontal motion of the right hinge, originating from inadvertent tightening of the nut-bolt pair at its interface with the actuator plate. As a result, anomalies appeared in the Force-Displacement diagram, attributable to the constrained degree of freedom and ensuing column displacement within the rigid stub. For specimens C3, C4, C5, C7, and C8 the tests were conducted without encountering any specific issues or complications. For specimen C6, failure occurred before completing the loading protocol, near the base

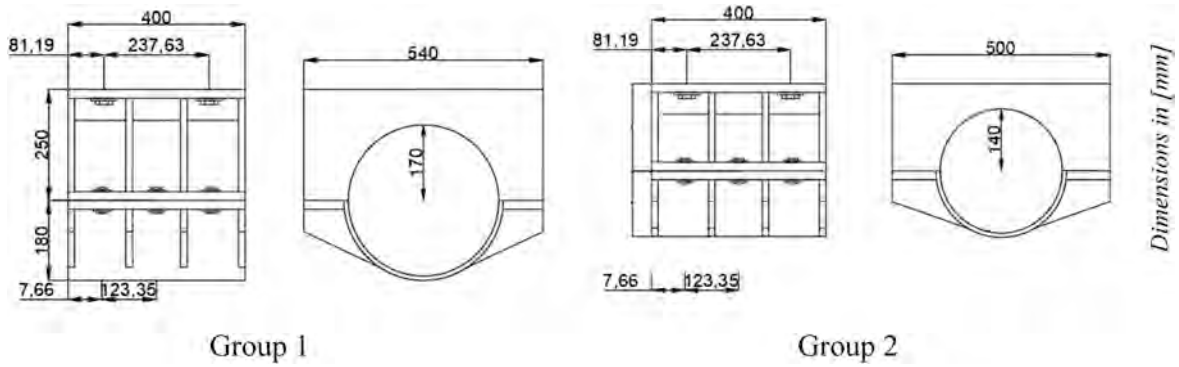

Fig. 5. Rigid stub scheme.

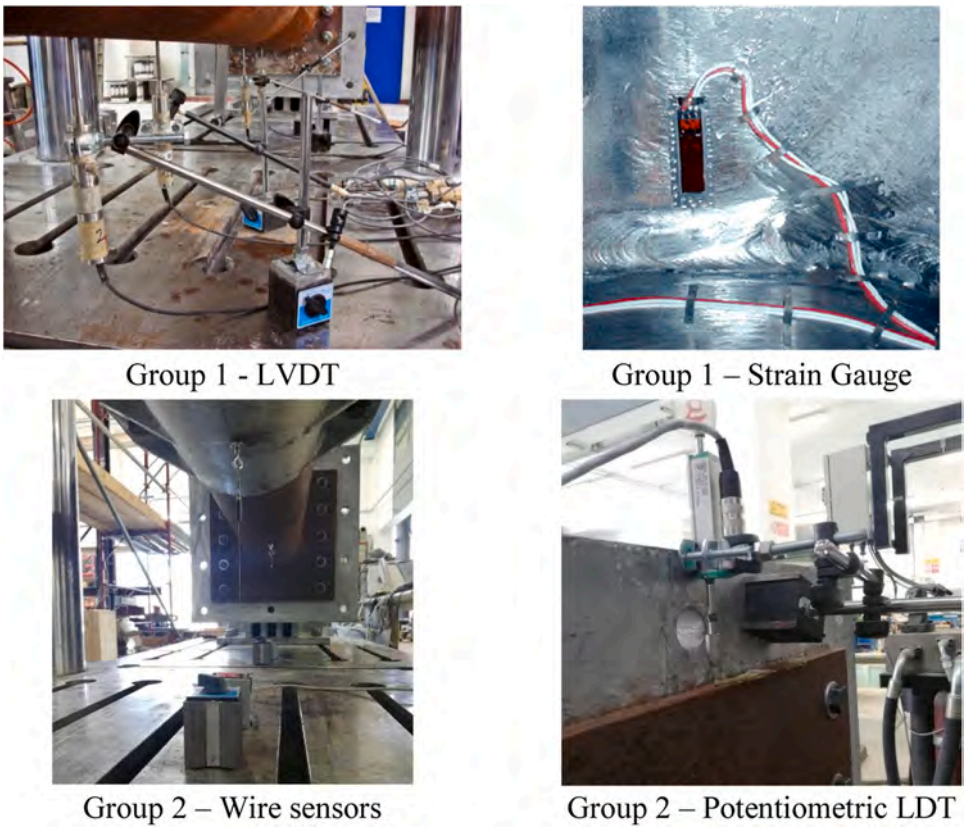

Fig. 6. displacement and deformation measurement instruments.

Table 2
Drift angle history of the cyclic test (C6, C8).

n. cycles	Drift angle [rad]
6	0.00375
6	0.005
6	0.0075
4	0.01
2	0.015
2	0.02
2	0.03
2	0.04
2	0.05
2	0.06
2	0.07
2	0.08
Until rupture	0.08

plate, likely due to a welding defect. Among the constant amplitude (CA) tests, a sudden drop in strength is noticeable in Group 1 (C1-C4) due to the high displacements applied (220 mm), inducing a significant exploiting of plastic resources from the initial cycles. This trend is less pronounced in specimens C5 and C7, characterized by a lower imposed displacement (140 mm).

In all the tests, it can be observed that near the points of intersection with the horizontal axis, there are non-harmonic segments in the Force – Displacement diagram. The formation of these segments can be attributed to the resistance provided by the bolts on the hinge base.

Table 5 reports some of the fundamental data characterizing the cyclic behaviour, such as the number of cycles to failure n_c, the number of cycles in the plastic range $n_{c,p}$, the maximum imposed displacement δ_{max}, the energy dissipated over the horizontal axis $E_{(+)}$, the energy dissipated below the horizontal axis $E_{(+)}$, their ratio, and the total dissipated energy E_t.

Fig. 7. Concrete specimens.

Table 3
Medium resistance of the concrete specimens.

Label	$F_{c.m}$ [kN]	$f_{c.m}$ [N/mm^2]
Cc1	987.6	43.31
Cc2	810.9	36.53
Cc3	989.8	44.29
Cc4	984.4	44.04
Cc5	938.5	39.85
Cc6	899.7	39.99
Cc7	986.6	43.27
Cc8	801.5	35.39

In addition, for the CFTs subjected to experimental tests under constant amplitude loading, graphs were obtained to analyse the degradation effects as a function of the number of cycles (k index), both in the positive and negative force quadrants Figs. 12–17. Specifically, the reaction force corresponding to the maximum/minimum displacement, divided by the imposed displacement $f_k^{(+,-)} = F_k^{(+,-)}/\delta_{\max}$ (taken as absolute value), the cumulative damage function $d_k^{(+,-)}$, and the interval damage $D_k^{(+,-)}$, have been defined as the number of cycles varies.

The cumulative damage function $d^{(+,-)}$ can be evaluated as:

$$d_k^{(+,-)} = 1 - \frac{f_k^{(+,-)}}{f_1^{(+,-)}} \tag{1}$$

where $f_k^{(+,-)}$is the reaction force corresponding to the maximum/minimum displacement, divided by the imposed displacement for the k-th cycle and $f_1^{(+,-)}$is the one referred to the 1st cycle.

It is also possible to define an equivalent damage function $d_{eq,k}^{(+,-)}$, considering the total damage between the first and the last values of $f_k^{(+,-)}$:

$$d_{eq,k}^{(+,-)} = \frac{d_{tot}^{(+,-)}}{n_c - 1} \bullet (k-1) \tag{2}$$

where $d_{tot}^{(+,-)} = 1 - \frac{f_{nc}}{f_1}$.

The values of $f_k^{(+,-)}$can be determined as follows:

$$f_k^{(+,-)} = \left(1 - d_k^{(+,-)}\right) \bullet f_1^{(+,-)} \tag{3}$$

Where $d_k^{(+,-)}$ can be also substituted by the equivalent cumulative damage $d_{eq,k}^{(+,-)}$.

The cumulative damage function $d_k^{(+,-)}$ and the equivalent damage $d_{eq,k}^{(+,-)}$ allow for the definition of $f_k^{(+,-)}$starting from the initial value $f_1^{(+,-)}$, without considering subsequent degradation steps. These quantities provide a measure of the accumulated damage over time, regardless of individual intervals.

On the other hand, the interval damage $D_k^{(+-)}$ and the average interval damage $E[D^{(+-)}]$ refer to the variation within a single interval $((k+1)-k)$.

$$D_k^{(+,-)} = 1 - \frac{f_k^{(+,-)}}{f_{k-1}^{(+,-)}} \tag{4}$$

The values of $f_k^{(+,-)}$, as a function of the interval damage $D^{(+-)}$, can be determined as follows:

$$f_k^{(+,-)} = \left(1 - D_k^{(+,-)}\right) \bullet f_{k-1}^{(+,-)} \tag{5}$$

In particular, the values of $f_k^{(+,-)}$ at the first $(k=1)$ and at the last cycle $(k = n_c)$ noted as $f_1^{(+)}, f_1^{(-)}, f_{nc}^{(+)}, f_{nc}^{(-)}$, the total damage $d_{tot}^{(+,-)}$, and the average value of the interval damage (valid for each cycle from the

Fig. 8. Geometry and uniaxial test in tension for dog bone specimens.

Table 4
Geometry and results of the experimental tests on dog bones.

Label	A_0 [mm^2]	A_f [mm^2]	f_y N/mm^2	f_{max} [N/mm^2]	f_t [N/mm^2]	$\varepsilon_{f_{max}}$ [-]	ε_{f_t} [-]	E [N/mm^2]	L_0 mm
C1-2	283.10	-	375	500.94	368.64	0.155	0.271	115000	90
C2-1	184.30	-	385	521.19	327.38	0.148	0.277	122000	90
C2-2	284.05	-	390	499.14	336.60	0.138	0.241	110000	90
C3-1	233.60	-	365	512.86	378.10	0.185	0.326	105000	90
C3-2	224.64	-	350	504.05	371.76	0.169	0.275	95000	90
C4-1	192.10	-	345	500.94	373.85	0.137	0.228	123000	90
C4-2	172.80	-	360	490.70	296.81	0.119	0.205	125000	90
C5-1	122.01	45.54	245	468.40	291.90	0.168	0.239	145000	90
C5-2	117.79	54.39	260	448.39	295.11	0.176	0.287	155000	90
C6-1	240.45	110.25	510	757.34	583.96	0.119	0.183	112000	90
C6-2	235.75	115.5	535	734.66	544.91	0.082	0.137	108000	90
C7-1	118.44	45.22	275	424.01	291.23	0.179	0.277	142000	90
C7-2	114.70	58.8	260	457.47	301.07	0.111	0.141	154000	90
C8-1	236.38	126.92	525	750.69	561.95	0.127	0.211	114000	90
C8-2	240.30	114.1	560	714.24	509.58	0.116	0.196	112000	90

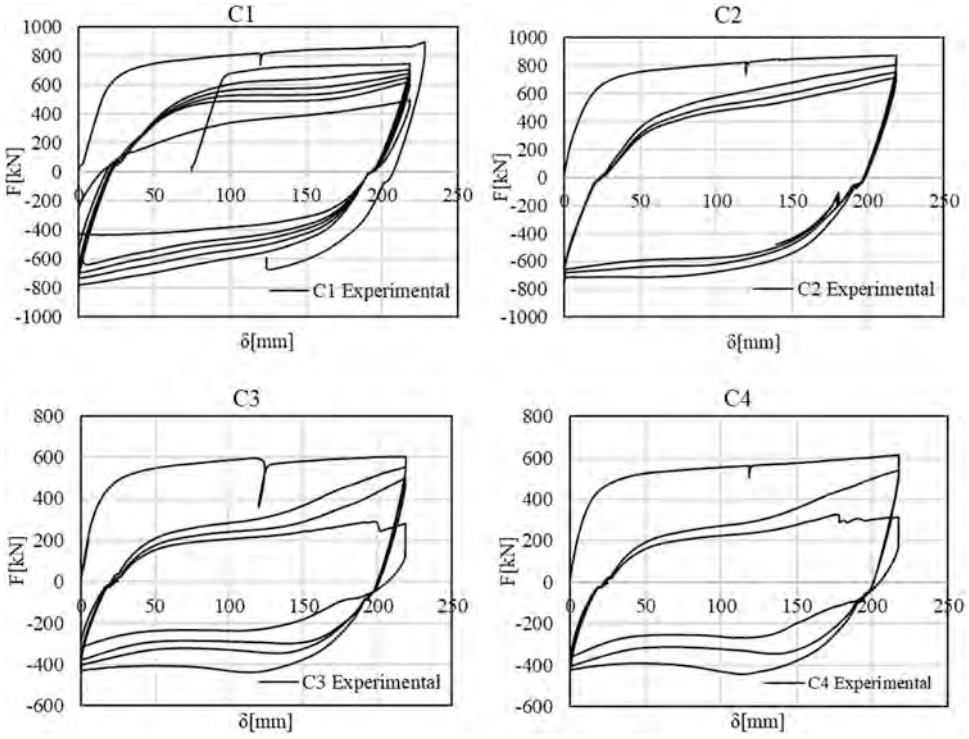

Fig. 9. Group 1 Experimental curves.

second to the last one) in both the quadrants $E[D^{(+)}], E[D^{(-)}]$, have been reported in Table 6.

Regarding the tests conducted under variable amplitude (C6-CV and C8-CV), the so-called skeleton curves have been derived. These curves are defined as the locus of peaks for each cycle, forming a geometric representation. Moreover, the secant stiffness, according to the displacement amplitude reported in Table 2, is shown in Figs. 18 and 19.

The ultimate (chord) rotation capacity has been derived for C6 and C8 specimens as follows:

$$R_u = \frac{\theta_u}{\theta_y} - 1 \tag{6}$$

Where θ_u is the ultimate rotation and θ_y is the yielding rotation.

The results are reported in Table 7.

5. Numerical validation of moment-curvature relationships using fibre model

The primary method for describing the nonlinear structural behaviour of a cross section is the moment-curvature relationship. Understanding this relationship is crucial for accurately estimating the ultimate strength and ductility of the section. In this section, the moment-curvature diagrams obtained from experimental tests using appropriately placed strain gauges on the specimens will be compared with a proposed numerical model. To evaluate the moment-curvature relationship, a fibre model has been applied, dividing the cross section into elementary areas with their corresponding uniaxial constitutive laws for confined concrete and steel. The subdivision was carried out through n angular increments $\Delta\alpha$. From this subdivision, the concrete core was divided into n circular sectors, while the tubular steel section was further divided into m parts along its thickness. Areas and centroids of these resulting figures were calculated to formulate equilibrium

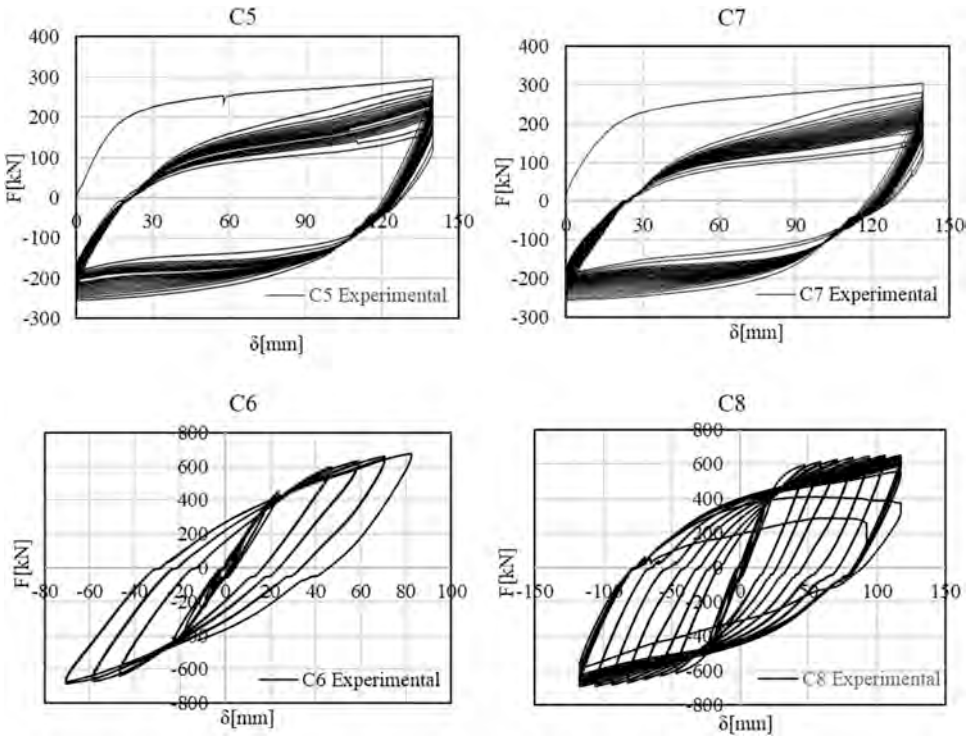

Fig. 10. Group 2 Experimental curves.

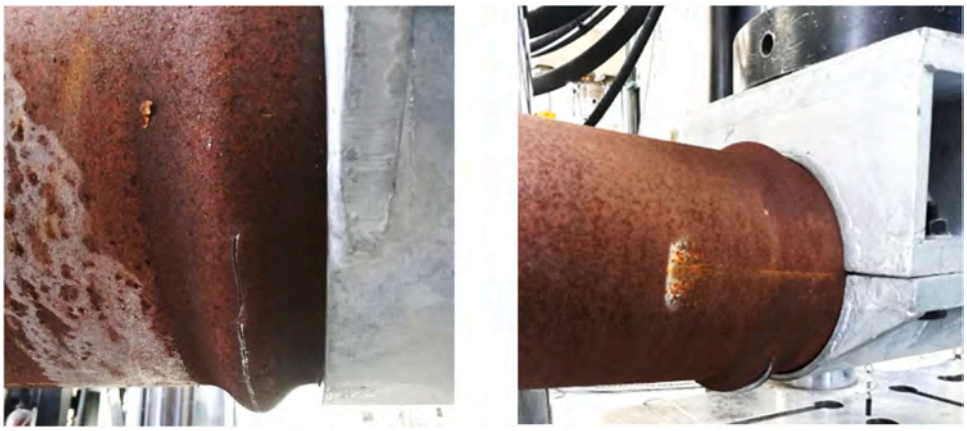

Fig. 11. Bulges and cracks near the rigid stub.

Table 5
Fundamental experimental data characterizing the cyclic behaviour of CFT.

Label CA	n_c [-]	$n_{c,p}$ [-]	δ_{max} [mm]	$E_{(+)}$ [kJ]	$E_{(-)}$ [kJ]	$E_{(+)}/E_{(-)}$ [-]	E_{tot} [kJ]
C1	7-6	7-6	220	824.146	522.673	1.577	1346.819
C2	4	4	220	445.908	317.806	1.403	763.714
C3	4	4	220	265.658	220.306	1.206	485.964
C4	3	3	220	213.751	169.939	1.258	383.690
C5	21-20	21-20	140	345.927	304.176	1.137	650.103
C7	24	24	140	420.939	369.680	1.139	790.619
VA							
C6	29	7	120.4	153.286	152.835	1.003	306.121
C8	48	24	120.4	1399.86	1291.104	1.084	2690.964

equations for translation and rotation as the sum of contributions from individual components. Certainly, as n and m increase, the outcome will increasingly demonstrate higher precision. The fibre model scheme is reported in Fig. 20.

The numerical evaluation of the moment-curvature diagram was conducted based on several assumptions:

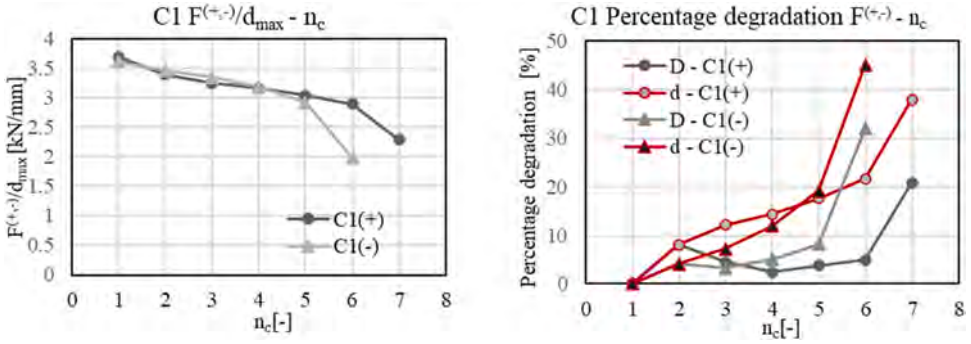

Fig. 12. C1 - $F^{(+,-)}/d_{max}$ - n_c and percentage interval (D) and cumulative (d) damage curves.

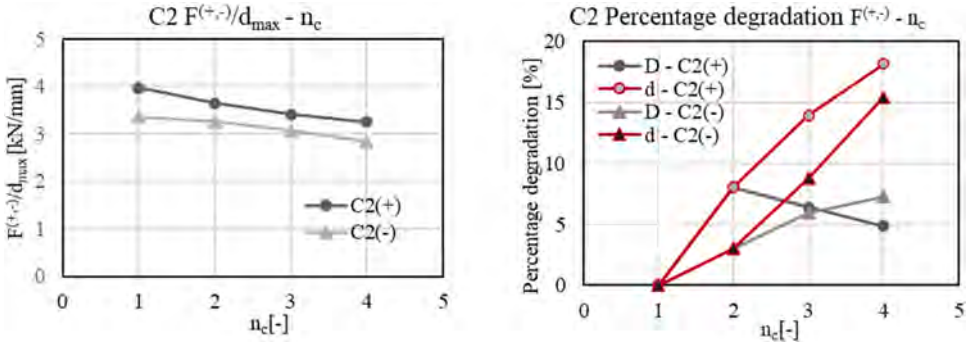

Fig. 13. C2 - $F^{(+,-)}/d_{max}$ - n_c and percentage interval (D) and cumulative (d) damage curves.

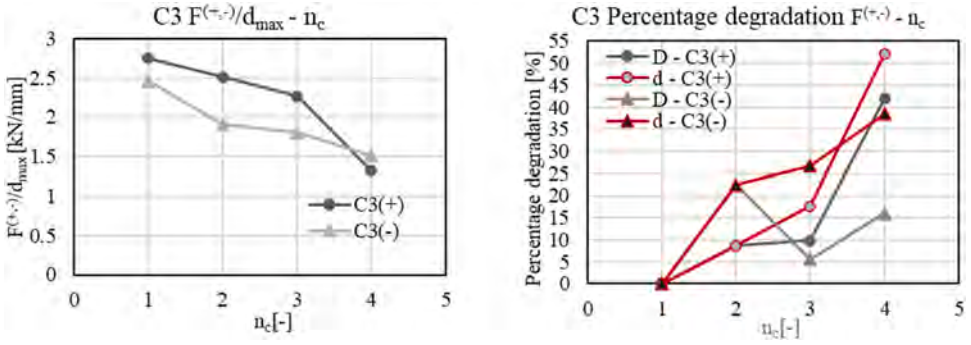

Fig. 14. C3 - $F^{(+,-)}/d_{max}$ - n_c and percentage interval (D) and cumulative (d) damage curves.

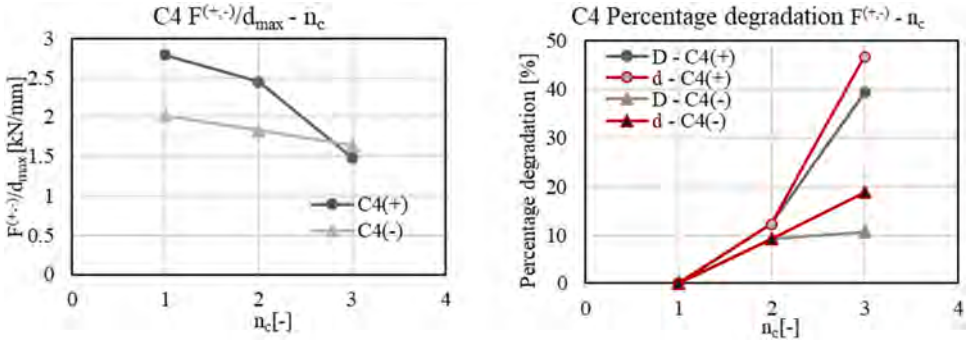

Fig. 15. C4 - $F^{(+,-)}/d_{max}$ - n_c and percentage interval (D) and cumulative (d) damage curves.

- interface adherence condition between steel and concrete until reaching the ultimate deformation of concrete;
- behaviour governed by the steel section once the ultimate deformation of concrete is exceeded;
- concrete not resistant to tension.

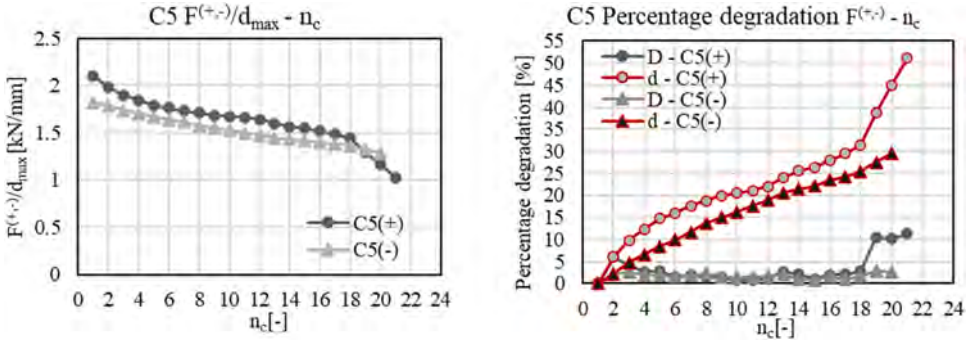

Fig. 16. C5 - $F^{(+,-)}/d_{max}$ - n_c and percentage interval (D) and cumulative (d) damage curves.

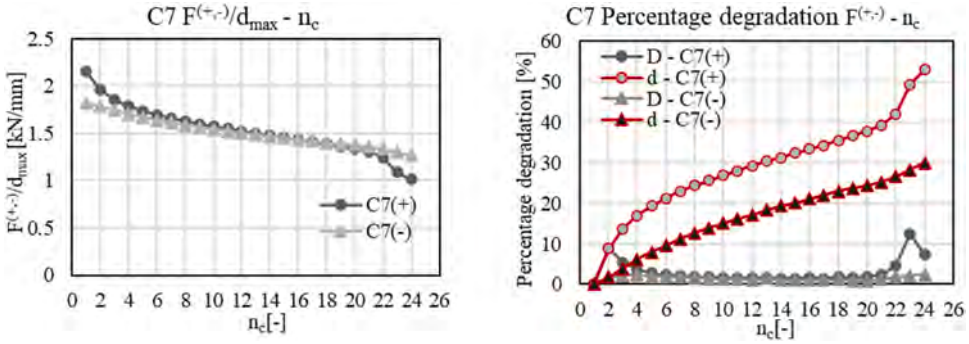

Fig. 17. C7 - $F^{(+,-)}/d_{max}$ - n_c and percentage interval (D) and cumulative (d) damage curves.

Table 6
Analysis experimental data characterizing the degradation under cyclic test of CFT.

Label	n_c	$f_1^{(+)}$	$f_{nc}^{(+)}$	$d_{tot}^{(+,)}$	$f_1^{(-)}$	$f_{nc}^{(-)}$	$d_{tot}^{(-)}$	$E[D^{(+)}]$	$E[D^{(-)}]$
CA	[-]	[kN/mm]	[kN/mm]	[%]	[kN/mm]	[kN/mm]	[%]	[%/Δn]	[%/Δn]
C1	7-6	3.69	2.28	37.99	3.61	1.98	45.13	7.43	10.56
C2	4	3.97	3.25	18.16	3.36	2.84	15.43	6.45	5.42
C3	4	2.75	1.32	52.10	2.46	1.51	38.47	20.11	14.66
C4	3	2.78	1.48	46.78	2.01	1.63	18.90	25.81	9.94
C5	21-20	2.11	1.03	44.87	1.83	1.29	29.46	3.45	1.82
C7	24	2.15	1.01	52.99	1.82	1.27	30.04	3.19	1.54

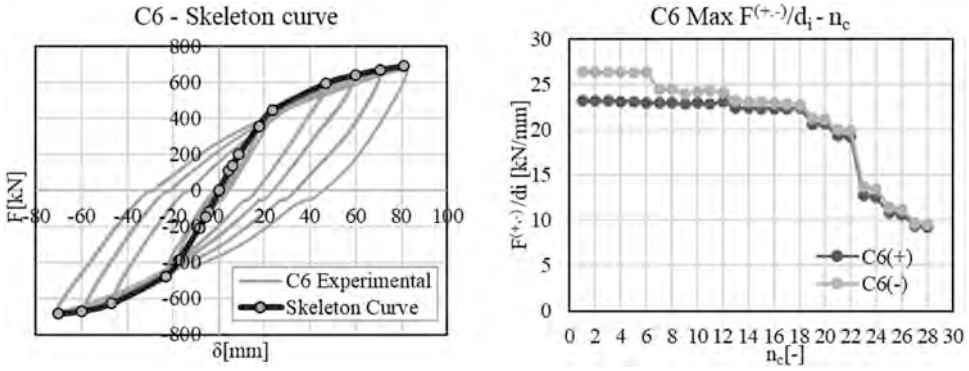

Fig. 18. C6 -skeleton and $F^{(+,-)}/d_i$ - n_c curves.

Given *i* as the subdivision index for $\Delta\alpha$ and *j* as the subdivision index within the thickness, the i-th contribution to the translational equilibrium can be expressed as follows:

$$N_i = A_{c,i} \bullet \sigma_{c,i} + \sum_{j=1}^{m} A_{sj,i} \bullet \sigma_{j,i} \tag{7}$$

where $A_{c,i}$ is the area of the i-th concrete core sector, $\sigma_{c,i}$ is the stress corresponding to the centroid of the concrete core sector, evaluated through the Mander Model, given the deformation, $A_{sj,i}$ is the area of the m-th part of the steel tube, pertaining to the i-th sector, and $\sigma_{j,i}$ is the corresponding stress, evaluated through the Ramberg-Osgood model, given the deformation.

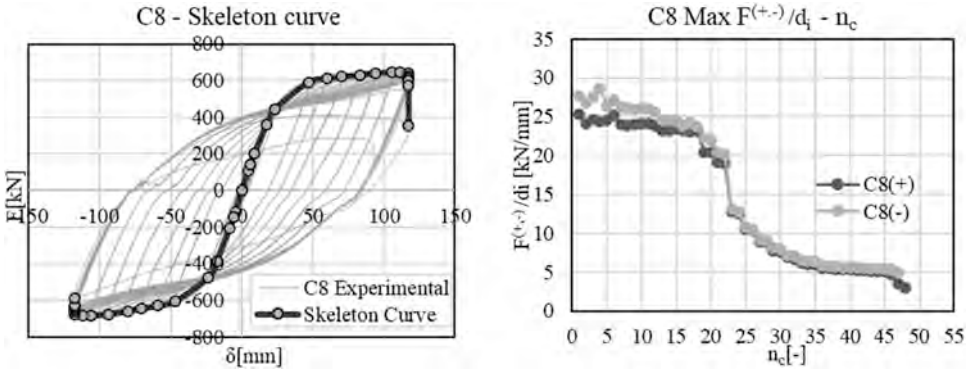

Fig. 19. C8 -skeleton and $F^{(+,-)}/d_i$ - n_c curves.

Table 7
Ultimate rotation capacity (C6, C8).

Specimen	θ_y [rad]	θ_u [rad]	R_u [-]
C6	0.0189	-	-
C8	0.0186	0.0933	4.01

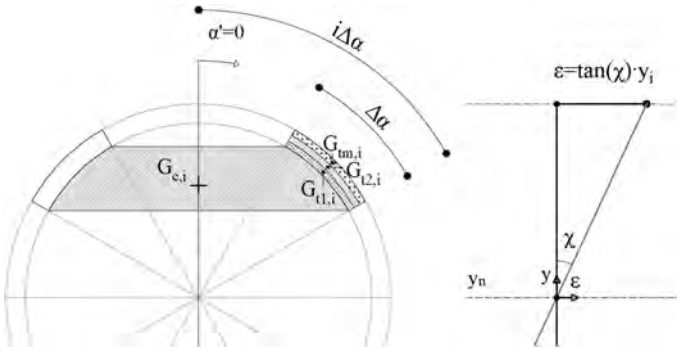

Fig. 20. Fibre model for the evaluation of Moment-Curvature law.

The i-th contribution to the rotational equilibrium respect to the barycentric axis can be written as:

$$M_i = A_{c,i} \bullet \sigma_i \bullet y_i + \sum_{j=1}^{m} A_{sj,i} \bullet \sigma_{j,i} \bullet y_{j,i} \tag{8}$$

where y_i is the centroid position of the i-th concrete core subdivision, and $y_{j,i}$ is the the centroid position of the j-th steel tube part of the i-th subdivision.

The procedure involves iteration. Beginning with a barycentric neutral axis and a defined curvature value χ, its position is iteratively adjusted until the difference between the internal and external normal stresses is below 2%. Once the neutral axis position is determined, it's possible to derive the corresponding bending moment and curvature. This process can be repeated by increasing or reducing the strain of the outermost fibre of the section to obtain the moment-curvature diagram.

For confined concrete, the stress-strain constitutive law proposed by Mander et al. [32,33] has been adopted, considering a lateral confining stress computed based on a circumferential stress in the steel tube equal to 0.10 f_y, as suggested in [34,35]. The stress-strain constitutive law for steel follows the classical Ramberg-Osgood [36,37] relationship, with different values for tension and compression to account for the biaxial stress state in the steel tube, according to the von Mises yield criterion [32–35].

The moment-curvature relationship is obtained through an iterative process for a given axial force. At each step, the curvature χ is fixed, and the strain distribution is determined iteratively by ensuring translational equilibrium. Once the strain diagram is known, i.e., the stress level of each elementary area is determined, the bending moment of the section is calculated using the rotational equilibrium equation.

The procedure terminates when one of the following conditions is met:

- One of the concrete elementary areas reaches the ultimate strain.
- One of the tensile steel areas reaches the ultimate strain.

5.1. Mander model for concrete

The confinement provided by the steel tube significantly enhances the strength and ductility of the concrete core. The confinement increases the lateral pressure on the concrete, restraining its outward.

The Mander model (1988) [32] is a well-established analytical formulation widely utilized to describe the confined behaviour of concrete in CFTs. It accounts for the effects of lateral pressure provided by the steel tube, accurately predicting the enhanced strength and ductility exhibited by.

Several studies have utilized the Mander model to analyse and design CFT structures. For instance, in [34] the Mander model has been exploited to simulate and predict the behaviour of CFT columns under bending. The study provided valuable insights into the confinement effects and the load-carrying capacity of CFT columns. The analytical formulation of the Mander model and its application in research and design have significantly contributed to the understanding and utilization of CFTs. By accurately representing the confined behaviour of concrete, the Mander model aids in optimizing the design and analysis of CFT structures, ensuring their reliable and efficient performance. The Mander model was originally proposed in 1988 and has since been widely adopted in research and engineering practice. The model incorporates stress-strain relationships and material parameters to represent the confined behaviour of concrete (Fig. 21). It has proven to be effective in predicting the stress-strain response and ultimate strength of confined concrete in CFTs.

The equations describing the model are reported in the following:

$$\sigma_c = \frac{f_{cc} x \quad r}{r - 1 + x^r} \tag{9}$$

$$f_{cc} = f_c \left(2.254 \sqrt{1 + \frac{7.94 f_l}{f_c}} - 2\frac{f_l}{f_c} - 1.254 \right) \tag{10}$$

$$\varepsilon_{cc} = 0.002 \left[1 + 5 \left(\frac{f_{cc}}{f_c} - 1 \right) \right] \tag{11}$$

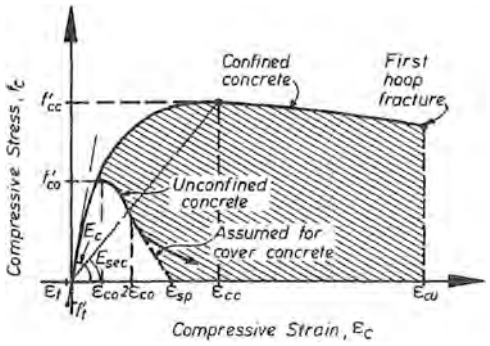

Fig. 21. Mander Model for Concrete [32].

$$x = \frac{\varepsilon_c}{\varepsilon_{cc}} \tag{12}$$

$$r = \frac{E_c}{E_c - E_{\text{sec}}} \tag{13}$$

$$E_{cc} = \frac{f_{cc}}{\varepsilon_{cc}} \tag{14}$$

$$E_c = 5000\sqrt{f_c} \quad (MPa) \tag{15}$$

Where σ_c and ε_c are the longitudinal compressive stress and strain of confined concrete f_c is the compressive (cylindric) strength of concrete ε_{cc} is the strain value corresponding to the achievement of the peak stress, f_{cc} is the confined compressive (cylindric) strength of concrete, E_{sec} is the secant modulus of confined concrete, f_y is the yield stress of the confining steel, and f_l is the lateral confinement stress, given by:

$$f_l = \frac{2\sigma_\theta \, t}{D} \tag{16}$$

Where σ_θ is the stress acting in the confining steel, t is the thickness of the tube, and D is the diameter.

Assuming the use of the Von Mises failure criterion [35], it is possible to consider the stress state of an infinitesimal element of a steel tubular section subject to global bending and interface interaction with concrete [35–40]. Based on these assumptions, it is possible to analyse a biaxial stress state characterized by principal stresses resulting from bending σ_v and hoop (confinement) stresses σ_θ. Specifically, according to experimental tests conducted by Azizzimini et al. [35], the representation of the plane stress state can be depicted as shown in Fig. 22.

From the analysis of the results, it can be stated that the axial compressive stress at the yielding state, f_{yc}, is lower than the yield stress in uniaxial conditions, f_y, whereas the tensile stress, f_{yt}, is higher than f_y. For $\sigma_\theta = 0.10f_y$, $f_{yt} = 1.05f_y$ and $f_{yc} = 0.95f_y$.

The confinement stress is of particular importance. If this parameter is equal to 0, Eq. (10) gives $f_{cc} = f_c$ (compressive resistance of confined concrete is the same as unconfined) and Eq. (11) gives $\varepsilon_{cc} = 0.002 = \varepsilon_{c0}$ which represents the strain corresponding to the maximum strength for unconfined concrete. The complete representation of the constitutive relationship for unconfined concrete is obtained by using Eq. (9) up to a strain equal to $2\varepsilon_{c0}$. From this strain level, it is necessary to calculate the

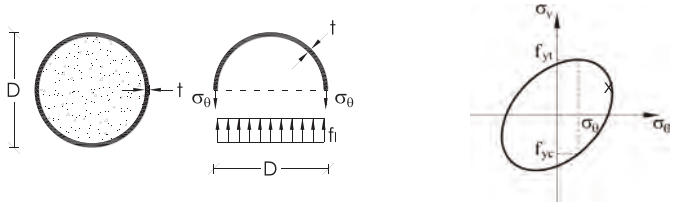

Fig. 22. Lateral confinement stress in Von Mises failure criterion.

tangent to the obtained curve and continue until it intersects the x-axis, determining the abscissa ε_{sp} representing the ultimate strain of unconfined concrete. The evaluation of the ultimate strain ε_{cu} can be performed according to the following relationship [32]:

$$\varepsilon_{cu} = 0.004 + 1.4\frac{\rho_s f_l \varepsilon_{fmax}}{f_{cc}} \tag{17}$$

where ρ_s is the confinement volumetric percentage ($\rho_s = 1$ in the CFT case).

5.2. Ramberg-Osgood model for steel

The Ramberg-Osgood model is widely used in the field of structural engineering to describe the nonlinear behaviour of steel materials under mechanical loading. This empirical model provides a valuable framework for understanding the stress-strain relationship beyond the elastic range. The model assumes that the stress-strain curve can be approximated by a power law expression, where the strain is related to the stress through a nonlinear relationship. The Ramberg-Osgood model is characterized by two material parameters: the yield strength and the hardening coefficient. The yield strength represents the stress at which plastic deformation begins, while the hardening coefficient determines the rate at which the material hardens with increasing strain.

The non-linear relationship between stress and strain can be expressed as follows:

$$\varepsilon = \frac{\sigma}{E} + K\left(\frac{\sigma}{E}\right)^n \tag{18}$$

where ε is the strain, σ is the stress, E is the Young's modulus, K and n are constants that depend on the material being considered.

Introducing the strength of the material f_0 corresponding to the yield offset, and defining a new parameter α as $\alpha = K(f_y/E)^{n-1}$, it is useful to rewrite Eq.(18) as follows:

$$\varepsilon = \frac{\sigma}{E} + \alpha\frac{f_0}{E}\left(\frac{\sigma}{f_0}\right)^n \tag{19}$$

where the term $a = \alpha\frac{f_0}{E}$ represents the yield offset characterizing the material.

5.3. Comparison between experimental and numerical M-χ curves

In this section, the proposed fibre model for the development of moment-curvature diagrams for CFT will be validated. Specifically, the validation will be conducted for Group 1 CFTs (C1-C4), for which strain gauges were applied to evaluate the deformations near the rigid stub. Given the geometry of the CFT, the position of the measurement devices relative to a fixed reference, and the boundary reactions, it was possible to define the moment-curvature diagrams based on the experimental tests.

Regarding the fibre model, the Ramberg-Osgood parameters characterizing the steel were calibrated through the results of tensile tests performed on the dog bone specimens (Table 4). The Ramberg-Osgood parameters can be found in Table 8.

As regards the Mander model for concrete, the unconfined concrete strength was taken as the average of the values presented in Table 3 ($f_c = 40.83N/mm^2$) and the hoop stress sigma theta was set as $\sigma_\theta = 0.1f_{\max}$ (steel). The remaining parameters required for characterizing the model can be found in Table 4.

Fig. 23 shows the moment-curvature comparison diagrams between the experimental tests and the fibre model.

To provide numerical evidence of what can be observed in Fig. 23, a comparison was made between the areas under the moment-curvature curves for both the experimental and fibre model curves. The results are presented in Table 9, demonstrating a high precision of the fibre

Table 8
Ramberg-Osgood parameters for Group 1 CFT.

Label	f_0 $[N/mm^2]$	n	$a = \alpha\frac{f_0}{E}$
C1	425	16	0.0045
C2	420	16	0.0085
C3	410	13	0.0089
C4	405	13	0.0078

model in capturing the monotonic $M-\chi$ behaviour. In fact, the percentage errors, always in favour of safety, ranged from 0.0319% to 3.72%.

The fibre model calibrated on the Group 1 CFTs (C1-C4) was extended to the Group 2 CFTs, for which strain gauge data were not available. Subsequently, for all CFTs, the ultimate bending moment (positive) evaluated through the fibre model was compared with the experimental one in Table 10.

5.4. Proposed fibre model vs experimental and fibre M-χ curves available in literature

To validate the proposed fibre model, comparisons were made with experimental curves and data sourced from existing literature. Notably, comparison was drawn to test data and fibre models previously introduced by Fujimoto et al. (2004) [31] and later by Liang et al. (2010) [30]. These studies involved testing CFTs under various Axial force P_n conditions. Table 11 provides an overview of the key parameters characterizing the analysed CFTs.

Table 9
Areas under $M-\chi$ curves - comparison.

Label	A_{exp} [Nmm • mm^{-1}]	A_{fiber} [Nmm • mm^{-1}]	Error [A] [%]
C1	40317.40	40094.77	0.552
C2	42043.36	41963.15	0.191
C3	24772.51	24764.60	0.0319
C4	26076.62	25106.50	3.72

Table 10
Ultimate bending moment – Fibre vs Experimental.

Label	$M_{u,exp}$ [kNm]	$M_{u,exp}$ [kNm]	Error [M_u] [%]
C1	525.5	523.2	0.438
C2	524.7	523.3	0.267
C3	372.3	371.1	0.322
C4	373.4	372.9	0.134
C5	185.7	188.1	1.276
C6	-	-	-
C7	188.6	189.3	0.370
C8	401.3	403.4	0.521

A first comparison has been made by assessing the mean (μ), standard deviation (SD), and coefficient of variation (COV) of the ratio between the ultimate bending moment derived through the fibre model and the experimental ultimate bending moment $M_{u,exp}$. In this comparison, M_{u1} and M_{u2} represent the ultimate moment values estimated by Fujimoto et al. [31] and Liang et al. [30] fibre models, respectively,

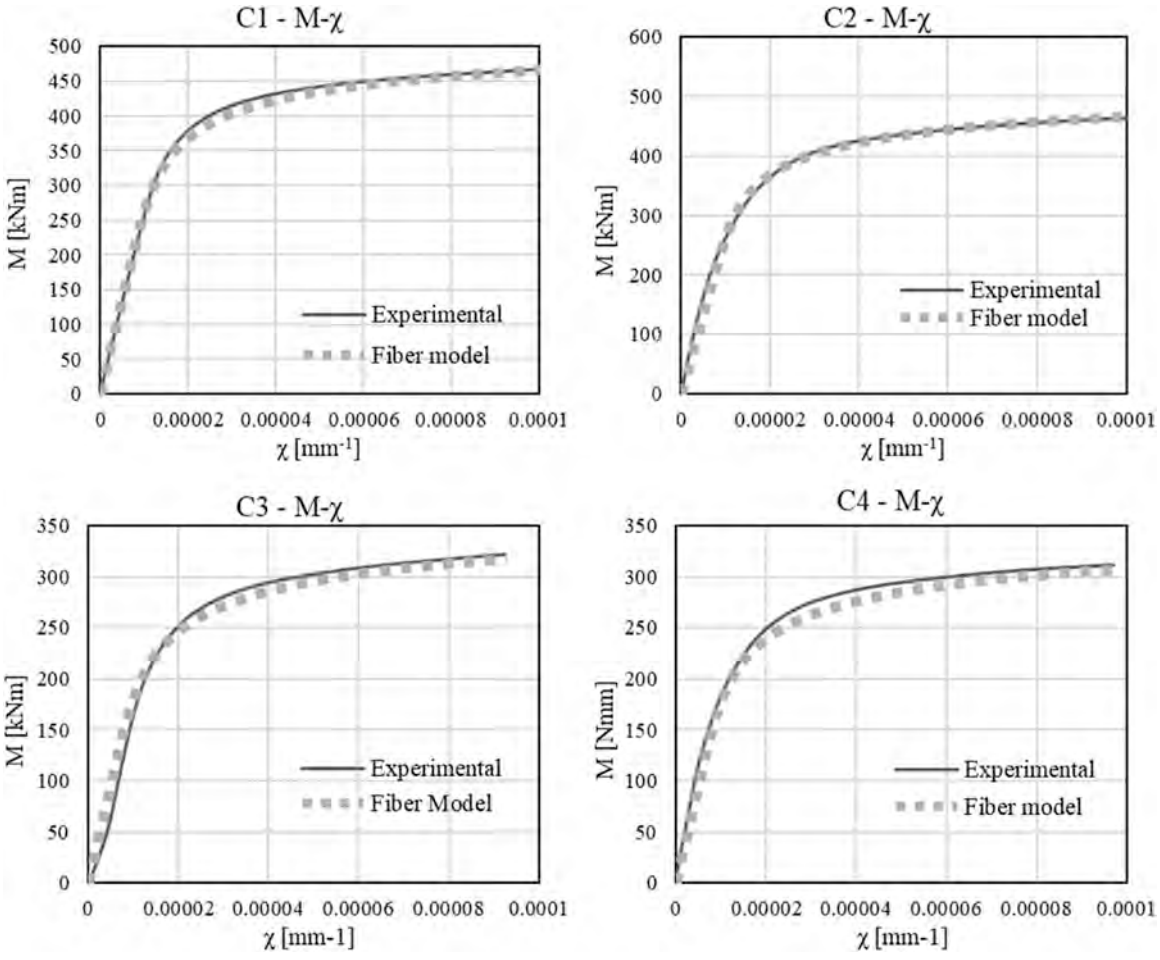

Fig. 23. C1 Experimental vs fibre model - Bending moment-curvature.

while M_{uf} represents the values estimated by the fibre model proposed in this study (Table 12), calibrating the parameters through the data reported in Table 11.

A second comparison has been conducted from a graphical standpoint. In Fig. 24, the comparison among the experimental curve, the proposed fibre model, and the fibre models by Fujimoto and Liang is presented. Specifically, the comparison is depicted for the curves analysed in [30]. In addition to a higher accuracy in the transition from the elastic to plastic phase, the proposed model shows an error in evaluating the area under the graph (compared to the area under the experimental curve) of a maximum of 3%, while models 1 and 2 range from 6% to 15% for the specimens under comparison.

6. Conclusions

This study presents an exhaustive investigation into the behaviour of Concrete-Filled Tubes (CFTs) under both monotonic and cyclic loading conditions in bending. Through experimental tests on eight specimens, critical insights into their structural performance have been obtained.

The results have been summarized in bullets:

- Cyclic behaviour of CFTs was characterized through parameters such as energy dissipation, number of cycles to failure, and maximum imposed displacement.
- This data is crucial for future finite element models seeking to accurately capture the cyclic behaviour of CFTs, energy dissipation, and force degradation over cycles.
- The study evaluated degradation effects and cumulative damage functions, providing a deep understanding of progressive damage and stiffness degradation in CFTs.
- For variable amplitude loading, skeleton curves were extrapolated, providing crucial insights into the structural response, such as the evolution of secant stiffness with varying cycles.
- High correlation between experimental bending moment-curvature curves and the fibre model was established, considering both the conducted tests and tests available in the literature.
- The proposed model has shown a COV for the ratio between fibre ultimate moment and experimental ultimate moment that is better than the models found in literature (from 0.05-0.08 to 0.025).
- The fibre model approach fits the experimental moment-curvature diagrams, with safety-favouring percentage errors ranging from 0.0319% to 3.72%.

In summary, this study significantly advances the understanding of CFTs under various loading conditions. It serves as a robust foundation for future research and finite element modelling, ensuring the safe and efficient application of CFTs in diverse engineering projects. Future research can extend these findings by exploring additional loading scenarios and long-term behaviour, thereby contributing to more sustainable and efficient engineering solutions.

Funding

All fundings have been acknowledged.

Ethical statement

This paper has not been previously published, is not currently submitted for review toany other journal and will not be submitted elsewhere during peer review for *Engineering Structures*.

CRediT authorship contribution statement

Montuori Rosario: Writing – review & editing, Supervision, Methodology, Conceptualization. **Nastri Elide:** Writing – review & editing, Validation, Supervision, Resources, Methodology, Data curation, Conceptualization. **Piluso Vincenzo:** Writing – review & editing, Validation, Supervision, Methodology, Data curation. **Todisco Paolo:** Writing – original draft, Validation, Software, Methodology, Investigation, Formal analysis.

Declaration of Competing Interest

The authors declare that they have no known competing financial interests or personal relationships that could have appeared to influence the work reported in this paper.

Table 11
Main parameters of CFTs tested reported in [30,31].

Specimen	D [mm]	t [mm]	D/t [-]	f_{sy} [N/mm^2]	f_{su} [N/mm^2]	E_s [N/mm^2]	f_c [N/mm^2]	P_n [kN]
EC4-A-4-03	150	2.96	50.7	283	408	224	40.7	359
EC4-C-2-035	300	2.96	101.4	283	408	224	25.4	840
EC4-C-2-06	300	2.96	101.4	283	408	224	25.4	1442
EC4-C-4-03	300	2.96	101.4	283	408	224	40.7	1060
EC4-C-4-04	300	2.96	101.4	283	408	224	40.7	1413
EC4-C-4-06	300	2.96	101.4	283	408	224	40.7	2120
EC4-C-8-045	300	2.96	101.4	283	408	224	78.1	2720
EC4-C-8-06	300	2.96	101.4	283	408	224	78.1	3627
EC6-A-4-02	122	4.54	26.9	579	646	228	40.7	273
EC6-A-4-06	122	4.54	26.9	579	646	228	40.7	817
EC6-C-2-06	239	4.54	52.6	579	646	228	25.4	1761
EC6-C-4-03	239	4.54	52.6	579	646	228	40.7	1077
EC6-C-4-06	239	4.54	52.6	579	646	228	40.7	2153
EC6-C-8-03	239	4.54	52.6	579	646	228	78.1	1556
EC6-C-8-06	239	4.54	52.6	579	646	228	78.1	3113
EC6-D-4-03	360	4.54	79.3	579	646	228	40.7	2050
EC6-D-4-06	360	4.54	79.3	579	646	228	40.7	4099
EC8-C-2-06	222	6.47	34.3	834	879	218	25.4	2684
EC8-C-2-08	222	6.47	34.3	834	879	218	25.4	3579
EC8-C-4-015	222	6.47	34.3	834	879	218	40.7	753
EC8-C-4-03	222	6.47	34.3	834	879	218	40.7	1506
EC8-C-4-06	222	6.47	34.3	834	879	218	40.7	3016
EC8-C-8-07	222	6.47	34.3	834	879	218	78.1	4421
EC8-D-4-045	336	6.47	51.9	834	879	218	40.7	3984

Table 12
Ultimate bending moment prediction and comparison [30,31].

Specimen	$M_{u,exp}$ [kNm]	M_{u1} [kNm]	M_{u2} [kNm]	M_{uf} [kNm]	$M_{u1}/M_{u,exp}$ [-]	$M_{u2}/M_{u,exp}$ [-]	$M_{uf}/M_{u,exp}$ [-]
EC4-A-4-03	32	29.9	29.3	30.5	0.934	0.916	0.953
EC4-C-2-035	128.3	128.9	123.6	128.5	1.005	0.963	1.002
EC4-C-2-06	109.7	104.2	103.2	110.1	0.950	0.941	1.004
EC4-C-4-03	150	157	149.1	151.8	1.047	0.994	1.012
EC4-C-4-04	156.6	154.9	148.6	154.3	0.989	0.949	0.985
EC4-C-4-06	130.5	122.5	120.2	126.6	0.939	0.921	0.970
EC4-C-8-045	194.1	218.3	208.9	205.7	1.125	1.076	1.060
EC4-C-8-06	160.8	173.7	171.2	165.4	1.080	1.065	1.029
EC6-A-4-02	46.9	46.4	44.7	47.1	0.989	0.953	1.004
EC6-A-4-06	42.2	37.3	38.5	41.9	0.884	0.912	0.993
EC6-C-2-06	132.3	149.1	140.7	138.7	1.127	1.063	1.048
EC6-C-4-03	177.6	195.2	189.2	184.9	1.099	1.065	1.041
EC6-C-4-06	155.4	153.7	151.9	154.1	0.989	0.977	0.992
EC6-C-8-03	217.3	229.3	221	217.2	1.055	1.017	1.000
EC6-C-8-06	178.2	175.8	178.4	181.3	0.987	1.001	1.017
EC6-D-4-03	460.5	488.8	473.3	480.7	1.061	1.028	1.044
EC6-D-4-06	399.6	369	371.2	386.9	0.923	0.929	0.968
EC8-C-2-06	219.8	236.3	217.7	219.1	1.075	0.990	0.997
EC8-C-2-08	149.3	170.9	149.6	149.9	1.145	1.002	1.004
EC8-C-4-015	301.7	314.9	297.1	299.4	1.044	0.985	0.992
EC8-C-4-03	282.3	306.5	292	287.2	1.086	1.034	1.017
EC8-C-4-06	261.3	247.2	243.5	256.5	0.946	0.932	0.982
EC8-C-8-07	262	254.3	264.4	262.2	0.792	1.009	1.001
EC8-D-4-045	648.1	685.3	653.8	650.8	1.057	1.009	1.004
Mean (μ)					**1.014**	**0.989**	**1.005**
SD					**0.084**	**0.049**	**0.025**
COV					**0.083**	**0.050**	**0.025**

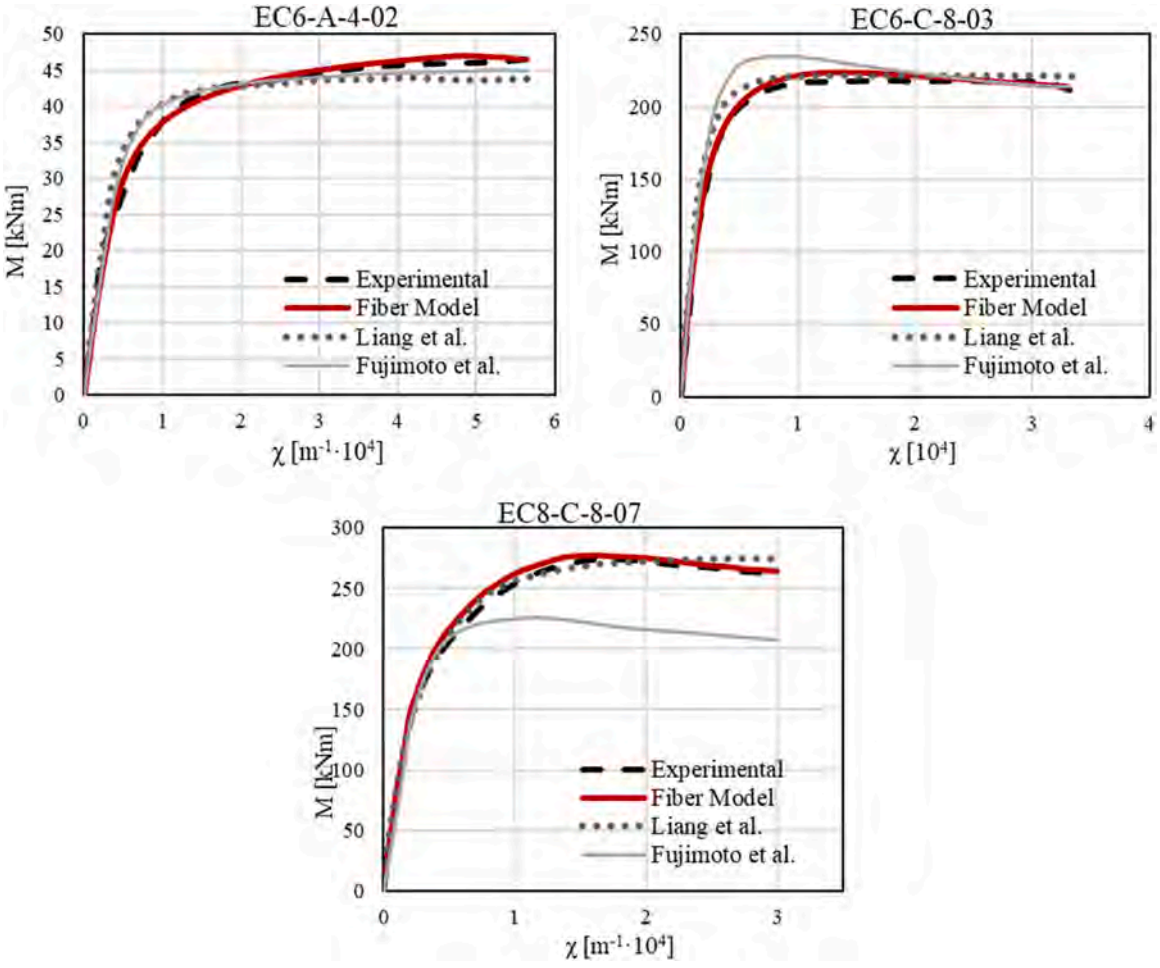

Fig. 24. Comparison between the experimental curve and the fibre models.

Data availability

The data that has been used is confidential.

Acknowledgements

None.

References

[1] Liu Q. Experimental and numerical study on the buckling behavior of concrete-filled steel tube columns. J Constr Steel Res 2018;145:281–95.
[2] Zhao XL, Han LH. Behavior and design of concrete-filled steel tubular structures. CRC Press; 2009.
[3] American Concrete Institute. (2019). ACI 318–19: Building Code Requirements for Structural Concrete.
[4] American Institute of Steel Construction, Inc. (AISC), In: Seismic Provisions for Structural Steel Buildings. ANSI/AISC Standard 341–10. AISC: Chicago, IN, USA, 2010.
[5] European Committee for Standardization. (2004). Eurocode 4: Design of composite steel and concrete structures - Part 1–1: General rules and rules for buildings. Brussels, Belgium: CEN.
[6] Wang X, Fan F, Lai J. Strength behavior of circular concrete-filled steel tube stub columns under axial compression: a review. Constr Build Mater 2022;322:126144. https://doi.org/10.1016/j.conbuildmat.2021.126144.
[7] Zhao Z, Wei Y, Wang G, Miao K, Zheng K. Exploration on unified calculation of axial compressive load-carrying capacity of square and rectangular concrete-filled steel tubular columns. Constr Build Mater 2023;398:132546. https://doi.org/10.1016/j.conbuildmat.2023.132546.
[8] Qing-li W, Hang-cheng G, Kuan P. Test on compressive performance of hollow concrete filled circular steel tube connected by thread through inner lining tube. Constr Build Mater 2023;370:130296. https://doi.org/10.1016/j.conbuildmat.2023.130296.
[9] Sangeetha P, Senthil R. Experimental behaviour of steel tubular columns for varying in filled concrete. Arch Civ Eng 2017;63(4):149–60. https://doi.org/10.1515/ace-2017-0046.
[10] Yu M, Liao W, Liu S, Wang T, Yu C, Cheng S. Axial compressive performance of ultra-high performance concrete-filled steel tube stub columns at different concrete age. Structures 2023;55:664–76. https://doi.org/10.1016/j.istruc.2023.05.113.
[11] Li Y-J, Han L-H, Xu W, Tao Z. Circular concrete-encased concrete-filled steel tube (CFST) stub columns subjected to axial compression. Mag Concr Res 2016;68(19):995–1010. https://doi.org/10.1680/jmacr.15.00359.
[12] Deng J, Zheng Y, Wang Y, Liu T, Li H. Study on axial compressive capacity of frp-confined concrete-filled steel tubes and its comparisons with other composite structural systems. Int J Polym Sci 2017;2017:6272754. https://doi.org/10.1155/2017/6272754.
[13] Zhang S, Miao K, Wei Y, Xu X, Luo B, Shi W. Experimental and theoretical study of concrete-filled steel tube columns strengthened by FRP/steel strips under axial compression. Int J Concr Struct Mater 2023;17(1):1. https://doi.org/10.1186/s40069-022-00556-2.
[14] Lai MH, Ho JCM. A theoretical axial stress-strain model for circular concrete-filled-steel-tube columns. Eng Struct 2016;125:124–43. https://doi.org/10.1016/j.engstruct.2016.06.048.
[15] Cao VV, Le PBN, Le KB, Nguyen LS. Behavior of circular concrete-filled steel tabular columns under monotonic and cyclic torsions. J Constr Steel Res 2023;210:108053. https://doi.org/10.1016/j.jcsr.2023.108053.
[16] St. Onge J, Fam A. Concrete-filled FRP tubes under combined torsion and bending. J Compos Constr 2022;26(6):04022073. https://doi.org/10.1061/(ASCE)CC.1943-5614.0001263.
[17] Elchalakani M, Zhao XL, Grzebieta RH. Concrete-filled circular steel tubes subjected to pure bending. J Constr Steel Res 2001;57(11):1141–68. https://doi.org/10.1016/S0143-974X(01)00035-9.
[18] Elchalakani M, Zhao X-L, Grzebieta R. Concrete-filled steel circular tubes subjected to constant amplitude cyclic pure bending. Eng Struct 2004;26(14):2125–35. https://doi.org/10.1016/j.engstruct.2004.07.012.
[19] Deng Y, Tuan CY, Zhou Q, Xiao Y. Flexural strength analysis of non-post-tensioned and post-tensioned concrete-filled circular steel tubes. J Constr Steel Res 2011;67(2):192–202. https://doi.org/10.1016/j.jcsr.2010.08.005.
[20] Zhou X, Zhan Y, Mou T, Li Z. Experimental research on flexural mechanical properties of ultrahigh strength concrete filled steel tubes. Materials 2022;15(15):5262. https://doi.org/10.3390/ma15155262.
[21] Deng Z, Sun T, Li J. Flexural performance of ultra-high performance concrete-filled high-strength steel tube beams. Tianjin Daxue Xuebao / J Tianjin Univ Sci Technol 2021;54(11):1111–20. https://doi.org/10.11784/tdxbz202012003.
[22] Li J, Deng Z, Sun T. Flexural behavior of ultra-high performance concrete filled high-strength steel tube. Struct Concr 2021;22(3):1688–707. https://doi.org/10.1002/suco.202000402.
[23] Ou J, Shao Y, Huang C, Chen Y, Bi X. Flexural behavior of circular concrete filled steel tubular members strengthened by CFRP sheets. Structures 2023;55:201–14. https://doi.org/10.1016/j.istruc.2023.06.031.
[24] İlgün A, Sancioğlu S. Flexural behaviour of different CFSTs cross-section shapes with the same steel cross-sectional area. Sadhana - Acad Proc Eng Sci 2023;48(2):53. https://doi.org/10.1007/s12046-023-02101-7.
[25] Abed F, Abdelmageed Y, Alhoubi Y. Effect of different cross-sections and concrete types on the flexural behavior of CFSTs. Compos Struct 2021;276:114570. https://doi.org/10.1016/j.compstruct.2021.114570.
[26] Ding F, Wu X, Xiang P, Yu Z. New damage ratio strength criterion for concrete and lightweight aggregate concrete. Acids Struct J 2021;118(6):165–78.
[27] Ding F, Liu Y, Fei L, Lu D, Chen J. Cyclic loading tests of stirrup cage confined concrete-filled steel tube columns under high axial pressure. Eng Struct 2020;221.
[28] Ding F, Pan Z, Lai Z, Yu Z. Experimental study on the seismic behavior of tie bar stiffened round-ended concrete-filled steel tube columns. J Bridge Eng 2020;25(10).
[29] Ding F, Yin G, Wang L, Hu D, Chen G. Seismic performance of a non-through-core concrete between concrete-filled steel tubular columns and reinforced concrete beams. Thin Walled Struct 2017;110:14–26.
[30] Liang QQ, Fragomeni S. Nonlinear analysis of circular concrete-filled steel tubular short columns under eccentric loading. J Constr Steel Res 2010;Volume 66(Issue 2):159–69. https://doi.org/10.1016/j.jcsr.2009.09.008.
[31] Fujimoto T, Mukai A, Nishiyama I, Sakino K. Behavior of eccentrically loaded concrete-filled steel tubular columns. J Struct Eng 2004;130(2):203–12. https://doi.org/10.1061/(ASCE)0733-9445(2004)130:2(203).
[32] Mander JB, Priestley MJN, Park R. Theoretical stress-strain model for confined concrete. J Struct Eng 1988;114(8):1804–26. https://doi.org/10.1061/(ASCE)ST.1943-541X.0002289.
[33] Hu Z, Wen Y, Wang B, Li X, Xu Y. Behavior of CFRP-confined concrete-filled square steel tube columns with section circularized under axial compression. Eng Struct 2022;252:113560. https://doi.org/10.1016/j.engstruct.2021.113560.
[34] Montuori R, Piluso V. Analysis and modelling of CFT members: moment curvature analysis. Thin Walled Struct 2015;86:157–66. https://doi.org/10.1016/j.tws.2014.10.010.
[35] Elremaily A, Azizinamini A. Behavior and strength of circular concrete-filled tube columns. J Constr Steel Res 2002;58(12):1567–91. https://doi.org/10.1016/S0143-974X(02)00005-6.
[36] Ramberg, W., Osgood, W.R. Description of stress–strain curves by three parameters, technical note no. 902, National Advisory Committee For Aeronautics: Washington, DC; 1943.
[37] Köllner A, Gardner L, Wadee MA. A new approach to the stability design of Ramberg–Osgood material struts. Structures 2023;56:104844. https://doi.org/10.1016/j.istruc.2023.07.034.
[38] Chen WF, Han DJ. Plasticity for structural engineers. J Ross Publ 2007.
[39] Lubliner J, Oliver J, Oller S, Oñate E. A plastic-damage model for concrete. Int J Solids Struct 1989;25:299–326. https://doi.org/10.1016/0020-7683(89)90050-4.
[40] Chen WF. Concrete plasticity: recent developments. Appl Mech 1994;47:S86–90. https://doi.org/10.1115/1.3124447.